Continuum Modeling of Inductor Magnetic Hysteresis and Eddy Currents in Resonant Circuits

Jason Pries, *Member, IEEE,* Emre Gurpinar, *Member, IEEE,* Lixin Tang, *Senior Member, IEEE,* Tim Burress, *Senior Member, IEEE*

***Abstract*—This paper presents a high-fidelity finite-element modeling technique for magnetic hysteresis and eddy current losses in toroid inductors. The method is based on the separation of ferromagnetic loss characteristics into two components: a quasi-static hysteresis component and a dynamic eddy current component. The Preisach model is used to describe the quasi-static magnetic hysteresis behavior of the core, providing strong guarantees on the reproducibility of the experimentally measured characteristics. This model is used to represent the magnetic field constitutive relationships within a finite-element framework combining the effects of hysteresis and eddy currents in a unified dynamic simulation. The finite-element model of the toroid is used as a high-order inductor model coupled to a resonant circuit simulation. The modeling technique is validated through experimental measurements on two different series RLC circuits. The first circuit is based on an M19 electrical steel toroid having resonant frequency near $200\,\mathrm{Hz}$. The second circuit is based on a T38 ferrite toroid having a resonant frequency near $10\,\mathrm{kHz}$. The models agree closely with the measured voltages, currents, and losses. The models also successfully predict discontinuities in the measured frequency responses due to the existence of bistable operating regimes.**

***Index Terms*—Magnetic hysteresis, eddy currents, RLC circuits, finite-element methods, magnetic losses**

I. Introduction

The macroscopic electromagnetic characteristics of ferromagnetic materials are the result of a set of intertwined phenomena occurring at several different length scales [1]–[3]. Predicting losses in ferromagnets can greatly aid in the design and optimization of electrical devices such as transformers, resonant circuits, and motors/generators. An overview of core losses and their physical origins can be found in [4]. Nonlinear amplitude variation, phase shifts, harmonic generation, and damping all greatly impact the accuracy of simulated resonant behavior compared to linear circuits. Unfortunately, simulating whole magnetic materials by fully coupling atomistic, domain, and bulk material scale phenomena is still a difficult problem even on today's most powerful supercomputers.

Purely mathematical models of macroscopically observed hysteresis exist independently—although often inspired by—the physical origins of magnetic hysteresis [5]. These methods abstract away details of the atomistic and domain scales while guaranteeing certain model characteristics and accuracy when identified from suitable experimental data. Mathematical models also permit separating quasi-static hysteresis behavior from the high-frequency eddy current phenomenon. It has been demonstrated that quasi-static scalar models of hysteresis may be extended to include frequency-dependent effects based on suitable analysis of Faraday's law [6]. This work shows that quasi-static hysteresis loops can be obtained as a limiting case of dynamic hysteresis models as frequency goes to zero.

Various analytical approximations of hysteresis loops have been explored in the context of finite-element simulations of power supply inductors, Epstein frames, magnetic recording, and planar magnetics [7]–[11]. Inverted Preisach models have been used in the context of two-dimensional simulations of electric motors [12]. A finite difference model coupled with a Preisach hysteresis model was used to analyze start-up errors in position identification of a switched reluctance motor caused by residual magnetization in the soft magnetic core [13]. Recently, a coupled finite-element Preisach hysteresis model was proposed for modeling laminated inductor cores, where special attention was paid to well-posedness of the problem and handling the lack of differentiability of the hysteresis operator [14]. Similarly, a one-dimensional Simulink model of a nonlinear inductor core was developed using an analytical expression for the hysteresis loops and validated on a full-bridge GaN-FET inverter with switching frequencies up to $500\,\mathrm{kHz}$ [15]. This work demonstrated the importance of accurately capturing eddy current losses when modeling cores over a wide frequency range.

Many investigations into coupled hysteresis/resonant circuit models have focused on the ferroresonance phenomenon observed in transformers. A parametric Preisach function was used to study the existence of bifurcations leading to a subharmonic resonant solution in an RLC circuit [16]. The authors noted this behavior was not apparent in models with single-valued magnetization curves. They raised a note of skepticism about using non-hysteretic inductor characteristic in the analysis of even the simplest of ferroresonant circuits. One-

J. Pries, E. Gurpinar, and T. Burress are with the Electrical and Electronic Systems Research Division of Oak Ridge National Laboratory, Oak Ridge, TN 37830, USA. L. Tang is with Karma Automotive LLC, Irvine, CA 92618, USA.

Corresponding author: Jason Pries, Research and Development Associate Staff Member, Oak Ridge National Laboratory, 1 Bethel Valley Road, P.O. Box 2008, MS-6472, Oak Ridge, TN, 37830, email: jason.pries@ieee.org, phone: 1-920-323-2962

This research used resources at the Power Electronics and Electric Machinery Research Facility, a DOE Office of Science User Facility operated by the Oak Ridge National Laboratory.

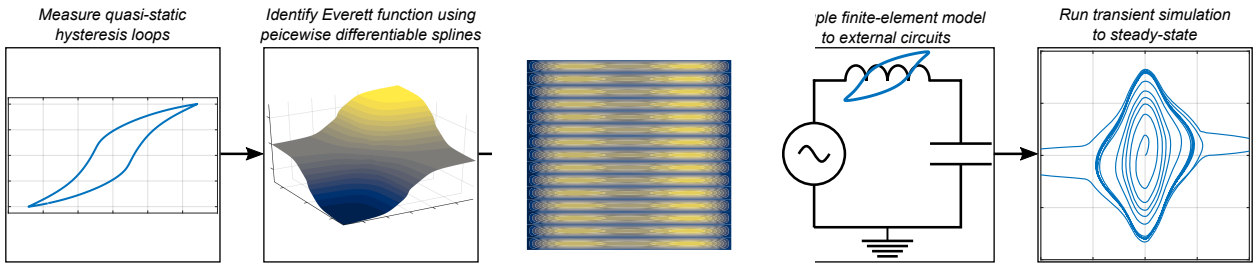

Fig. 1. Steps for constructing the resonant circuit model coupled with a high-fidelity inductor simulation included hysteresis and eddy currents

dimensional finite-element models in Cartesian coordinates coupled with a Preisach hysteresis model have been used to investigate bifurcation and bistability characteristics of RLC circuits in the context of amplitude and frequency modulation of the supply voltage [17]. A comparative study showed that, despite having similar major loops, simulations of noise-induced (stochastic) resonance in nonlinear systems produced vastly different results depending on the type of hysteresis model [18]. This result emphasizes the need to carefully validate models in the context of relevant phenomenon.

This paper presents a method for constructing high-fidelity finite-element models of toroid inductors and coupling them to external circuits [19]. The quasi-static magnetic hysteresis characteristics of the inductor core is captured using the Preisach hysteresis model and is identified from a set of low-frequency major loop measurements. The experimental data are compressed using piecewise differentiable splines to ensure differentiability and fast evaluation of the history dependent nonlinear operator. The core geometry and material conductivity are used to construct a finite-element model to capture eddy currents at higher frequencies. The procedure for tracking the history of the magnetization state at the quadrature points is described so that high-order basis functions can be employed to improve computational efficiency. The method for coupling the field-based inductor model to external circuits is detailed. These measurement and modeling steps are outline in the flowchart in Fig. 1.

The method is validated using experimental measurements performed on two different resonant circuits—one using an M19 electrical steel toroid and the other a T38 ferrite toroid. Importantly, the experimental validation is out of sample: Because of the resonant behavior, the voltage and current waveforms are different (non-sinusoidal) than the ones used to identify the model (sinusoidal average flux). The simulations accurately predict the nonlinear frequency response of both circuits, tracking changes in resonant frequency and quality factor as the source voltage is varied. The model also successfully predicts measured frequency response discontinuities and related bistable operating regions in both the electrical steel and ferrite resonant circuits.

II. Hysteresis

The quasi-static hysteresis characteristics of ferromagnetic toroid inductors can be accurately modeled using a scalar Preisach model. Identifying such models requires measuring major hysteresis loops over a range of peak flux density values. The measurements must be taken at a frequency low enough so that the loops appear constant with respect to small variations in frequency. This requirement ensures that eddy currents have a negligible effect on the observed macroscopic hysteresis loops. The measurement frequency range can be determined by requiring that the skin-depth of the material is much larger than the height and radial width of the inductor core.

We assume the core material has an associated nonlinear function describing the relationship between field intensity H and flux density B given by

$$B = \mu_o \left(H + M \left(H \right) \right). \tag{1}$$

The magnetization state M of the core represents the nonlinear part of the B-H relationship. The value $\mu_o M$ is referred to as the magnetic polarization. Assume we have a set of major loop measurements $\left(H_m \left(t \right), M_m \left(t \right) \right)$ at a frequency $f = 1/T$. For simplicity, we assume the ascending branch of the hysteresis loop occurs for $t \in [0, T/2]$ and the descending branch for $t \in [T/2, T]$. The minimum and maximum values of $M_m \left(t \right)$ occur at $t = 0$ and $t = T/2$.

The scalar Preisach model assumes the output state of a material exhibiting hysteresis can be described by an integral over a two-dimensional space tracking the internal state of a distribution of hysterons (i.e., two state relays). Let $\gamma_{\alpha,\beta}$ be the hysteron that switches to a value of $+1.0$ for $x > \alpha$ and -1.0 for $x < \beta$. The output of the Preisach hysteresis model with density function $\mathcal{P}$ is

$$y = \int_{\mathcal{S}_+} \mathcal{P} \left(\alpha, \beta \right) d\alpha d\beta - \int_{\mathcal{S}_-} \mathcal{P} \left(\alpha, \beta \right) d\alpha d\beta, \tag{2}$$

where $\mathcal{S}_+$ is the set of all (α, β) such that $\gamma_{\alpha,\beta} = +1.0$, and $\mathcal{S}_-$ is the set of all (α, β) such that $\gamma_{\alpha,\beta} = -1.0$. A hysteron with $\beta > \alpha$ is typically thought to be nonphysical for ferromagnetic materials and $\mathcal{P} \left(\alpha, \beta \right) = 0$ is assumed in this region. The asymmetric switching of individual hysterons produces internal memory and is the cause of hysteresis observed on a macroscopic scale. The continuous distribution of hysterons ensures a smooth output variation with the applied field [5].

Direct determination of $\mathcal{P}$ is difficult because of the need to differentiate noisy experimental data twice. However, the measured major hysteresis loop ascending and descending branches can be transformed directly into an equivalent Everett function model. The Everett function $\mathcal{E} \left(\alpha, \beta \right)$ is given by

$$\mathcal{E} \left(H_m \left(0 \right), H_m \left(t \right) \right) = M_m \left(t \right) - M_m \left(0 \right) \tag{3}$$

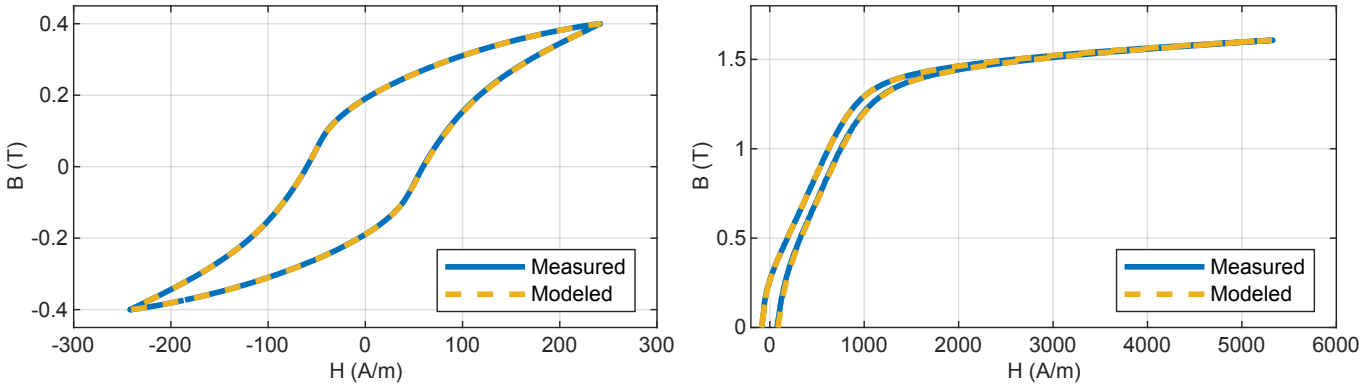

(a) 400 mT (b) 1.6 T

Fig. 2. Modeled and measured M19 hysteresis loops at an excitation frequency of 5 Hz and flux density amplitudes of (a) 400 mT and (b) 1.6 T.

for the ascending branch with $t \in [0, T/2]$ and

$$\mathcal{E}\left(H_m\left(T/2\right), H_m\left(t\right)\right) = M_m\left(t\right) - M_m\left(T/2\right) \tag{4}$$

for the descending branch descending with $t \in [T/2, T]$. In words, the line (x, y) described by $y = \mathcal{E}\left(h, x\right)$ for $h > 0$, $x \in [-h, h]$ is exactly the ascending hysteresis loop branch measured for the peak field h shifted by the corresponding peak magnetization. The Preisach density function can be calculated from the Everett function as

$$\mathcal{P} = -\frac{\partial^2 \mathcal{E}}{\partial\alpha\partial\beta}. \tag{5}$$

The state of a scalar Preisach system is completely described by a set of past input extrema. The line defined by $\mathcal{L}\left(t\right) = \mathcal{S}_+ \bigcap \mathcal{S}_-$ associated with the waveform $H\left(\tau\right)$ for $\tau \in [0, t]$ is composed of a set of horizontal and vertical links whose vertices generate a sequence of N_n values $\{H^n\}$. Using this sequence, the magnetization state at time t is given by

$$M = -\frac{1}{2}\mathcal{E}\left(-H^{max}, H^{max}\right) + \sum_{n=1}^{N_n - 1} \mathcal{E}\left(H^n, H^{n+1}\right), \tag{6}$$

where $H^{N_n} = H\left(t\right)$ and H^{max} is the maximum absolute value of $\{H^n\}$. The exact method required to track the evolution of $\mathcal{L}\left(t\right)$ given $H\left(t\right)$ is described in [5].

Two measured hysteresis loops are given in Figs. 2a and 2b for a toroid core constructed of several sheets of M19 electrical steel. The measurements were taken at 5 Hz to minimize frequency-dependent effects. Bézier splines were used to interpolate the Everett function between measured values after the experimentally measured hysteresis loop data was filtered to remove noise. At both low and high flux density levels, the Everett function faithfully reproduced the measured behavior.

III. Eddy Currents

The macroscopically observed B-H loops of ferromagnetic materials are known to widen as excitation frequency increases. This is due to the development of eddy currents in the material body as the skin depth decreases below the smallest dimension of the sample perpendicular to the field direction. This phenomenon is not hysteresis—it appears in nonmagnetic materials such as copper—but it *is* an additional source of core losses. Quasi-static hysteresis loops can roughly be considered a property of the bulk material, whereas the way the loops widen with frequency depends on the geometry of the sample.

The main equations used to describe the field dynamics in this work are Ampere's law,

$$\nabla \times \vec{H} = \vec{J}, \tag{7}$$

and Faraday's law,

$$\nabla \times \vec{E} = -\frac{\partial \vec{B}}{\partial t}. \tag{8}$$

Toroidal cores can be modeled in axisymmetric coordinates with H_θ and B_θ as the only non-zero components of the field intensity and flux density. Restricting our attention to the interior of the core and assuming ohmic conduction,

$$\vec{J} = \sigma\vec{E}, \tag{9}$$

with material conductivity σ, we may rewrite Ampere's law,

$$\sigma E_r = -\frac{\partial H_\theta}{\partial z}, \tag{10}$$

$$\sigma E_z = \frac{1}{r}\frac{\partial r H_\theta}{\partial r}, \tag{11}$$

and Faraday's law,

$$-\frac{\partial B_\theta}{\partial t} = \frac{\partial E_r}{\partial z} - \frac{\partial E_z}{\partial r}. \tag{12}$$

Combining (10)–(12) produces

$$\sigma\frac{\partial B_\theta}{\partial t} = \frac{\partial^2 H_\theta}{\partial z^2} + \frac{\partial}{\partial r}\frac{1}{r}\frac{\partial r H_\theta}{\partial r}, \tag{13}$$

which is simply the nonlinear diffusion equation

$$\sigma\frac{\partial B_\theta}{\partial t} = \nabla^2 H_\theta \tag{14}$$

in axisymmetric coordinates.

Equation (13) is solved using finite-element analysis. Given shape functions w_i, the corresponding weight functions are

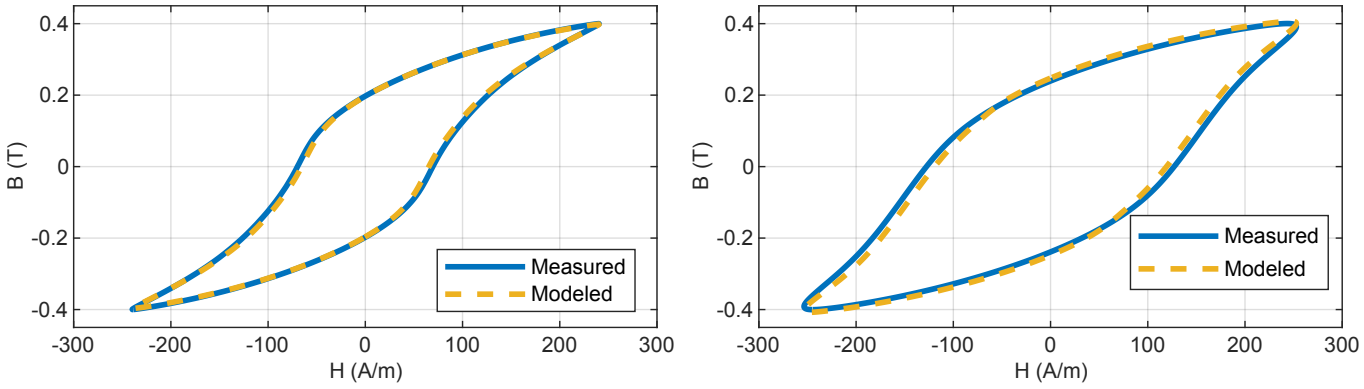

(a) 50 Hz (b) 500 Hz

Fig. 3. Modeled and measured M19 hysteresis loops with amplitudes of 400 mT at excitation frequencies of (a) 50 Hz and (b) 500 Hz

chosen to be rw_i. Multiplying (13) by rw_i and integrating over the core cross section Ω gives

$$\int_\Omega rw_i\sigma\frac{\partial B_\theta}{\partial t}drdz = \int_\Omega rw_i\frac{\partial^2 H_\theta}{\partial z^2}drdz + \int_\Omega rw_i\frac{\partial}{\partial r}\frac{1}{r}\frac{\partial rH_\theta}{\partial r}drdz. \tag{15}$$

The domain $\Omega = [r_{id}, r_{od}] \times [-h_z/2, h_z/2]$ where r_{id} and r_{od} are the inner and outer radius, respectively, and h_z is the core height. Using integration by parts on (15) and expanding the partial derivatives with respect to r reveals the corresponding symmetric weak form:

$$\int_\Omega w_i\sigma\frac{\partial B_\theta}{\partial t}rdrdz + \int_\Omega \frac{\partial w_i}{\partial z}\frac{\partial H_\theta}{\partial z}rdrdz + \int_\Omega \left(\frac{\partial w_i}{\partial r}+\frac{w_i}{r}\right)\left(\frac{\partial H_\theta}{\partial r}+\frac{H_\theta}{r}\right)rdrdz = 0. \tag{16}$$

The field solution is approximated as

$$H_\theta(r,z) = \sum_j w_j H_j, \tag{17}$$

where H_j are the interpolated field intensity values for node j. Our implementation uses a single element and a high-order polynomial basis to obtain an accurate field representation. This strategy has the benefit of faster convergence as the polynomial order is increased, which reduces the number of unknowns and Preisach model evaluations required for a specified accuracy [20].

The integrals in (16) are evaluated using numerical quadrature with quadrature points (r_q, z_q) and quadrature weights ω_q. The integrals are advanced in time using the implicit-Euler method with fixed time step Δt and time $t^k = t^{k-1} + \Delta t$. Before application of boundary conditions, this yields the following equation:

$$F\frac{B^k - B^{k-1}}{\Delta t} + KH^k = 0. \tag{18}$$

The vector $H^k = \{H_j^k\}$ contains the nodal field intensity values. The vector $B^k = \{B_q^k\}$ contains flux density values at the quadrature points, which are generally different from the node locations. The entries of the matrix F are the values of the integrand of the first term in (16) evaluated at the quadrature points and multiplied by the quadrature weights

$$F_{i,q} = \sigma w_{i,q} r_q \omega_q. \tag{19}$$

The entries of the matrix K are given by

$$K_{i,j} = \sum_q \frac{\partial w_{i,q}}{\partial z}\frac{\partial w_{j,q}}{\partial z}r_q\omega_q + \left(\frac{\partial w_{i,q}}{\partial r}+\frac{w_{i,q}}{r_q}\right)\left(\frac{\partial w_{j,q}}{\partial r}+\frac{w_{j,q}}{r_q}\right)r_q\omega_q. \tag{20}$$

The notation $w_{i,q}$ is used to indicate the value of the function w_i (or its partial derivative) evaluated at quadrature point q.

The discretized problem is advanced in time by solving the nonlinear equation using Newton's method. To do this, it is necessary to calculate the differential permeability μ_q from the slope of the active branch of the hysteresis loop at the quadrature points. This is done by directly evaluating the first partial derivative of the Everett function:

$$\mu_q = \frac{\partial B_q}{\partial H_q} = \mu_o\left[1 + \frac{\partial \mathcal{E}}{\partial \beta}\left(H_q^{N_n-1,k}, H_q^{N_n,k}\right)\right], \tag{21}$$

where $H_q^{N_n-1,k}$ and $H_q^{N_n,k}$ are the quadrature point link values associated with $\mathcal{L}$ described in Section II at time t^k. Following linearization, entries of the Jacobian $\mathcal{J}$ are given by the following expression:

$$\mathcal{J}_{i,j} = K_{i,j} + \sum_q \frac{\sigma\mu_q}{\Delta t} w_i w_j r_q \omega_q. \tag{22}$$

Dirichlet boundary conditions are applied by assuming the current in the inductor winding applies a field intensity to the boundary of the core. Let H_Γ^k be the values of H^k on the boundary of Ω. When $H_j^k \in H_\Gamma$, the value is prescribed by the applied primary current I^k:

$$H_j^k = \frac{N_t}{2\pi r_j} I^k, \tag{23}$$

where N_t is the number of turns, and r_j is the radius of node j. After application of the boundary conditions, (18) becomes

$$F_d\frac{B^k - B^{k-1}}{\Delta t} + K_d H^k = DI^k. \tag{24}$$

The matrices F_d and K_d are adapted from F and K, respectively, by setting the rows associated with the core boundary values to zero, except the corresponding diagonal entries of K which become 1. The vector D translates the forcing current I^k into the boundary field values using (23). The relationship between the winding current and the field boundary values provides a mechanism for coupling the field equations to circuit models as described in the next section.

The loop widening phenomena is demonstrated on the M19 toroid for an excitation frequency of 50 Hz in Fig. 3a and 500 Hz in Fig. 3b. Compared to the 5 Hz loop in Fig. 2a, the 50 Hz loop is nearly unchanged. On the other hand, the 500 Hz loop encloses a significantly larger area, indicating an increase of losses per cycle. Observe in Fig. 3b that, for a fixed flux density amplitude, the apparent coercivity of the material increases.

IV. Resonant Circuit Coupling

A series RLC resonant circuit with a nonlinear inductor can be described by a set of ordinary differential equations:

$$I - C\frac{\partial V_c}{\partial t} = 0, \tag{25}$$

$$\frac{\partial \lambda}{\partial t} + RI + V_c = V_s\left(t\right). \tag{26}$$

The voltage induced by the flux in the core is modeled as a nonlinear flux-linkage λ, which is implicitly a function of H. The induced voltage can be written as the integral of the time derivative of B over Ω scaled by the number of turns N_t and—in the case of laminated cores—the number of laminations N_l:

$$\frac{\partial \lambda}{\partial t} = N_t N_l \int_\Omega \frac{\partial B}{\partial t} dr dz. \tag{27}$$

This allows the circuit equations to be driven by the continuum field model in Section III. After discretizing in time, we arrive at the following equations:

$$I^k = C\frac{V_c^k - V_c^{k-1}}{\Delta t}, \tag{28}$$

and

$$S\frac{B^k - B^{k-1}}{\Delta t} + RI^k + V_c^k = V_s\left(t^k\right). \tag{29}$$

The vector S is a discrete version of the integral operator in (27) with entries given by

$$S_q = N_t N_l \omega_q. \tag{30}$$

The solution is advanced in time using Newton's method to solve the coupled field-circuit equations represented by (24), (28), and (29). Doing this requires linearizing the first term in (29) with respect to the field intensity. The corresponding entries of the Jacobian are given by $\mathcal{J}_{\lambda,j}$:

$$\mathcal{J}_{\lambda,j} = N_t N_l \sum_q \frac{u_q}{\Delta t} w_j \omega_q. \tag{31}$$

TABLE I
M19 Inductor Resonant Circuit Properties

ID	OD	Height	σ	N_t	R_{dc}	C
50.8 mm	62.1 mm	5.25 mm	4.85 $\frac{\text{MS}}{\text{m}}$	460	1.16 Ω	9.88 µF

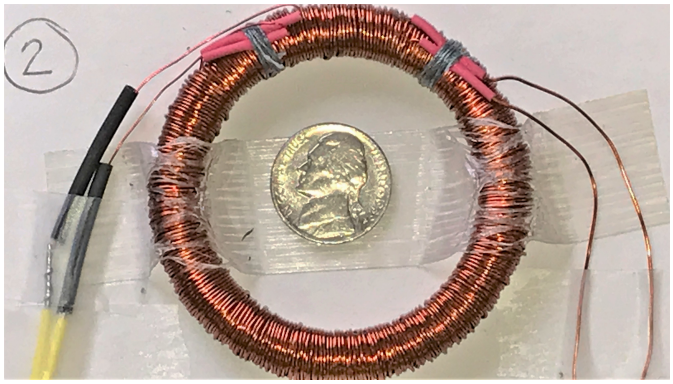

Fig. 4. M19 toroid inductor.

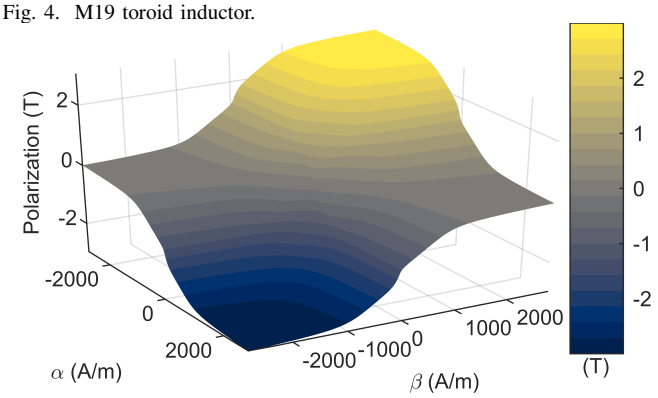

Fig. 5. Measured Everett function for the M19 toroid.

V. Experimental Results

We now compare the accuracy of two different models constructed using the proposed technique. The first inductor is made of M19 electrical sheet steel laminations and is deployed in a circuit operating at resonance near 200 Hz. The second is a ferrite toroid of T38 ferrite material by TDK in a circuit operating at resonance near 10 kHz. We focus our attention on how the models capture shifts in the resonant frequency and quality factor since these values depend critically on the nonlinear inductance and losses.

A. M19 Electrical Steel Core

The first circuit uses an inductor made of M19 electrical steel. The core consists of a stack of 15 laminations that are each approximately 0.35 mm thick. The as wound inductor is depicted in Fig. 4. The core was originally designed to conform to the ASTM A773/A773M-01 ring core standard [21]. A 10 µF capacitor was chosen to locate the resonant frequency of the system near 200 Hz based on a representative inductance value. Table I lists the key measured inductor and resonant circuit characteristics. The measured M19 Everett function is depicted in Fig. 5.

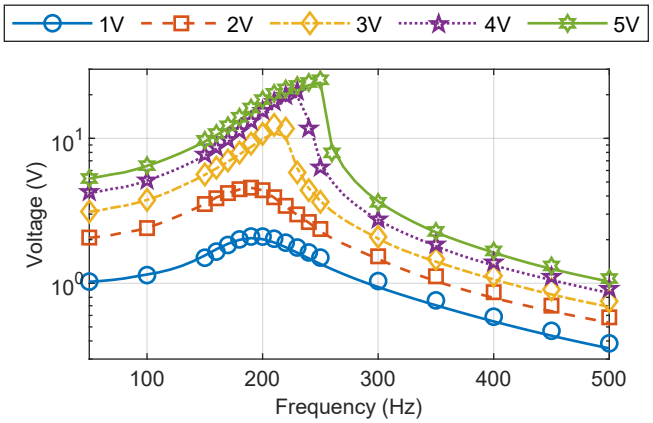

(a) Capacitor RMS Voltage

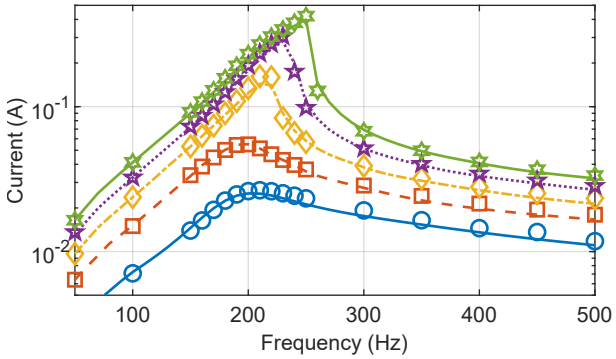

(b) Inductor RMS Current

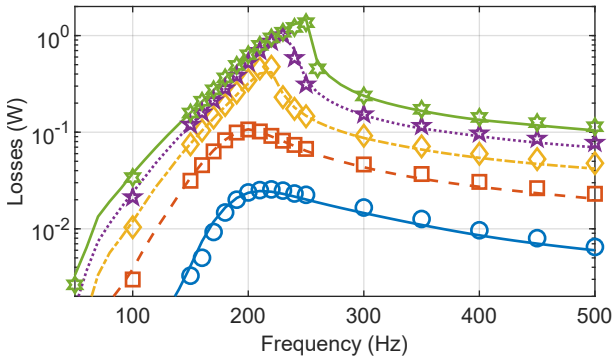

(c) Total Losses

Fig. 6. Comparison of simulated and measured M19 resonant circuit frequency responses as a function of input voltage.

The voltage source amplitude was swept from $1\,\mathrm{V_{RMS}}$ to $5\,\mathrm{V_{RMS}}$. The source frequency was swept from $50\,\mathrm{Hz}$ to $500\,\mathrm{Hz}$. The simulated and measured values of the capacitor RMS voltage, inductor RMS current, and total circuit input power are shown in Fig. 6. The simulation results capture several important trends observed in the experimental results related to location of the resonant peak and changes in the quality factor. The resonant peak is observed to shift from $190\,\mathrm{Hz}$ at $1\,\mathrm{V_{RMS}}$ to $250\,\mathrm{Hz}$ at $5\,\mathrm{V_{RMS}}$. The measured quality factor—determined as the ratio of input voltage to capacitor voltage—shifts from 2.10 to 5.07 at these points, versus the predicted values of 2.05 and 4.85, respectively. The accuracy of the quality factor mirrors the accuracy of the simulated losses as demonstrated in Fig. 6c.

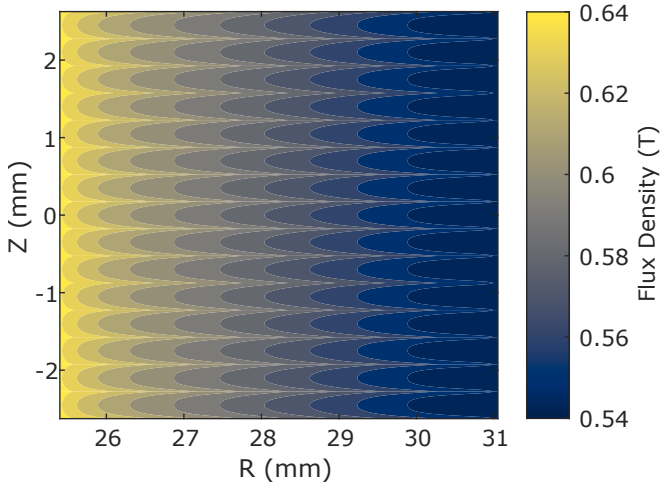

(a) RMS flux density

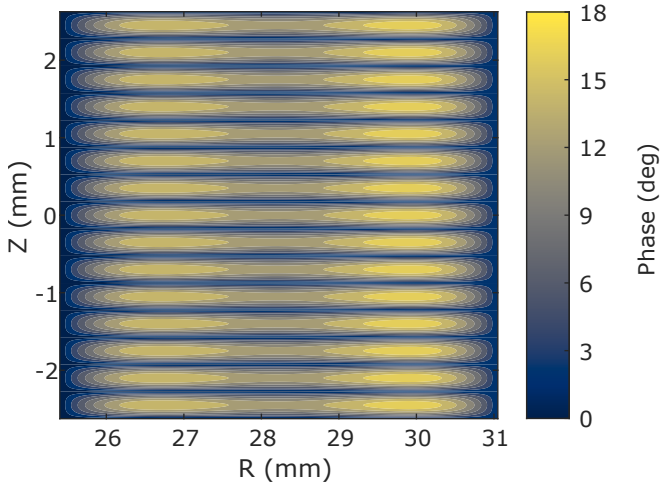

(b) Phase of fundamental flux density harmonic

Fig. 7. Simulated flux density in the M19 inductor core for an input voltage of $5\,\mathrm{V_{RMS}}$ and frequency of $250\,\mathrm{Hz}$.

The simulated RMS flux density and phase of the fundamental harmonic are depicted in Fig. 7 for the $5\,\mathrm{V_{RMS}}$, $250\,\mathrm{Hz}$ operating point. Nonuniformity of the RMS flux density is due to two factors: the difference in magnetic path length at the outer and inner diameter of the core and eddy currents. In Fig. 7a, the variation in the flux density amplitude is more significant in the r-direction than in the z-direction. This is primarily due to magnetic path length differences. Eddy currents have a more significant impact on the phase of the magnetic flux density in the interior of the core. The phase shift of the magnetic field causes the apparent inductance of the core to drop even when the flux density amplitude is unchanged. The two lobes observable in the phase plot of Fig. 7b are the result of eddy currents on the inner and outer diameter of the inductor core and the larger core radial thickness compared to the material skin depth at this frequency.

B. T38 Ferrite Toroid

The second circuit is designed with a ferrite toroid core using TDK's T38 material. The target resonant frequency of

TABLE II
T38 INDUCTOR RESONANT CIRCUIT PROPERTIES

ID	OD	Height	σ	N_t	R_{dc}	C
13.7 mm	22.1 mm	7.90 mm	62 $\frac{S}{m}$	22	60 mΩ	69.1 nF

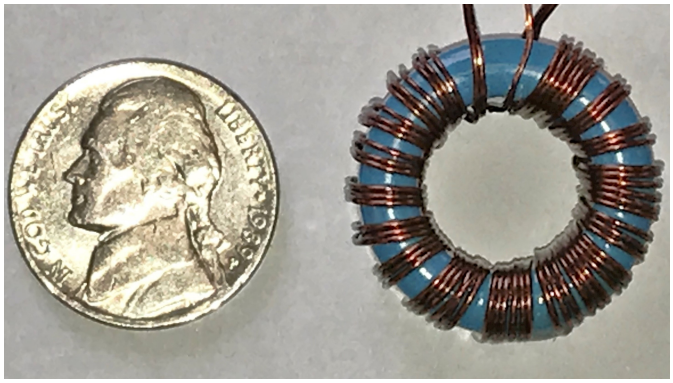

Fig. 8. T38 toroid inductor.

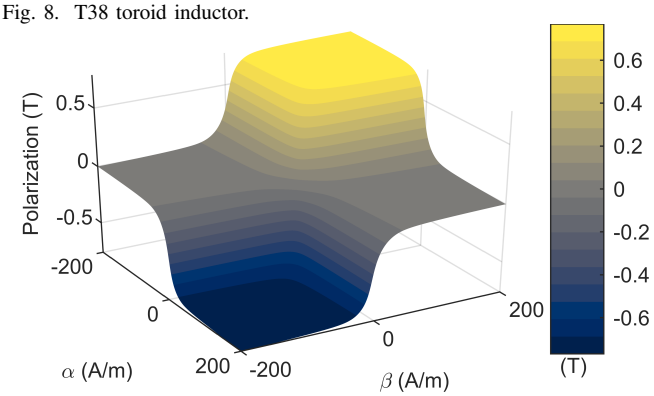

Fig. 9. Measured Everett function for the T38 ferrite core.

this circuit was set at 10 kHz. The core size and material were chosen so that the skin-depth of the material at 10 kHz—based on data sheet information—is approximately equal to two times the core height at 10 kHz. This ensures that eddy currents are an appreciable part of the total circuit losses. Otherwise, a comparison would only judge the quasi-static model accuracy and have little to do with the dynamic behavior. The core was wound with 26 AWG magnet wire so that the copper losses should be nearly frequency independent over the measurement range. The relevant inductor and capacitor properties are listed in Table II.

The Everett function identified using this core is shown in Fig. 9. The measured and simulated capacitor RMS voltage, inductor RMS current, and total circuit input power are shown in Fig. 10. The source voltage amplitude is swept from 1 V_{RMS} to 3 V_{RMS}. The source frequency is swept between 2 kHz and 20 kHz. Again, good agreement between the simulated and measured trends are observed. The capacitor voltage gain at a source amplitude of 1 V_{RMS} and frequency of 8.5 kHz is measured to be 4.13 versus a predicted value of 4.44 At a source amplitude of 3 V_{RMS} and frequency of 11 kHz, the measured capacitor gain increases to 4.27 versus a predicted value of 4.70 The measured losses, as shown in Fig. 10c,

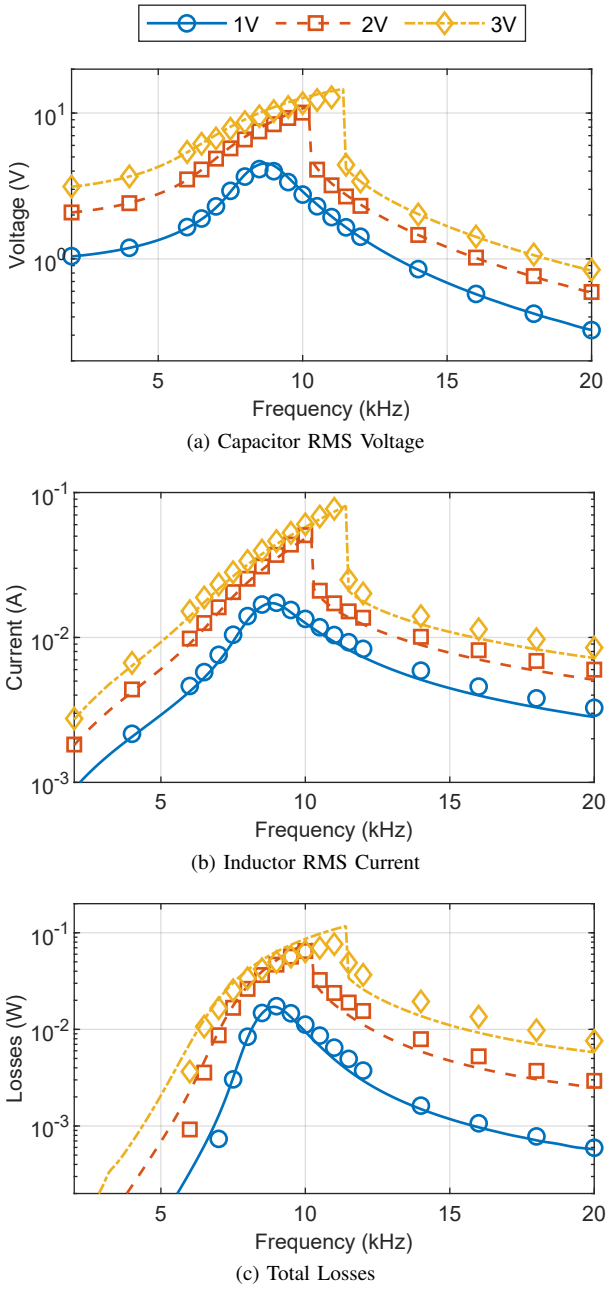

(a) Capacitor RMS Voltage

(b) Inductor RMS Current

(c) Total Losses

Fig. 10. Comparison of simulated and measured T38 resonant circuit frequency responses as a function of input voltage.

are in good agreement with predicted values. The predictions tend to be more accurate at lower frequencies. A similar trend is observed in the inductor RMS currents in Fig. 10b. This suggests that, the core inductance is being overestimated at higher frequencies, limiting the current and losses in the simulation model when the capacitor impedance is small.

The simulated RMS flux density and phase of the fundamental harmonic are depicted in Fig. 11 for the 3 V_{RMS} 11 kHz operating point. Like the M19 core, nonuniformity of the RMS flux density in the T38 core as shown in Fig. 11a is more severe in the r-direction than in the z-direction. The slight bowing of the contour lines is due to the core eddy currents. Eddy currents also greatly affect the phase of the fundamental harmonic as shown in Fig. 11b. Compared to the M19 core

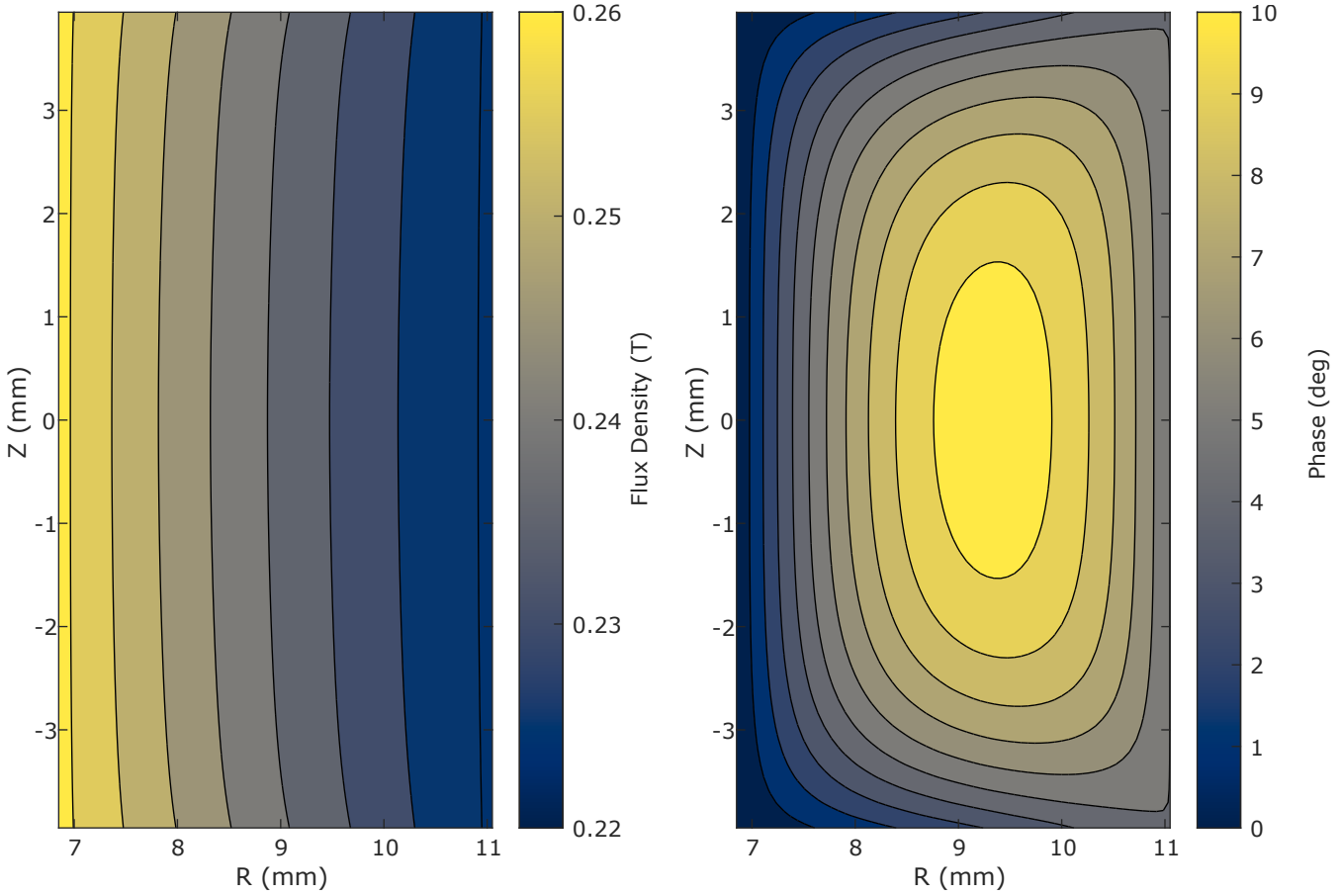

(a) RMS flux density

(b) Phase of fundamental flux density harmonic

Fig. 11. Simulated flux density in the T38 inductor core for an input voltage of $3\,\mathrm{V_{RMS}}$ and frequency of $11\,\mathrm{kHz}$.

flux density phase in Fig. 7b, the T38 core flux density does not have any lobes in the distribution. This is because the T38 core cross section is relatively squarer (with an aspect ratio of 1.88 to 1) compared to a single M19 lamination cross section (with an aspect ratio of 1 to 16.1).

VI. Bifurcation and Bistability

Both resonant circuits exhibit discontinuities in their frequency responses in Figs. 6 and 10, especially at higher input voltages. These resonant circuits can be viewed as a dynamic system described by the nonlinear equation

$$\frac{\partial x}{\partial t} = f\left(x\,;v_s,f_s\right), \tag{32}$$

where $x = \{i, v\}$ is the state vector consisting of the inductor current and capacitor voltage, and v_s and f_s are system parameters describing the source applied voltage and frequency, respectively. Under reasonable assumptions on the initial conditions of the system, the solutions of (32) tend toward periodic orbits $x = \Phi\left(t\,;v_s,f_s\right)$ with

$$\Phi\left(t\,;v_s,f_s\right) = \Phi\left(t+T_s\,;v_s,f_s\right), \tag{33}$$

and $T_s = 1/f_s$. Examining, for example, the $3\,\mathrm{V_{RMS}}$ applied voltage data in Fig. 10a, a discontinuous change of the capacitor voltage occurs as the frequency is varied near $11\,\mathrm{kHz}$. This manifests as a discontinuous change in the steady-state periodic orbit Φ as f is varied. A related phenomenon of bistable operation can be observed as v_s is varied.

A. Steady-State Periodic Orbits Bifurcations

Figs. 12 and 13 show measured and simulated phase portraits, respectively, for the M19 resonant circuit at both $250\,\mathrm{Hz}$ and $260\,\mathrm{Hz}$. Similarly, Figs. 14 and 15 show measured and simulated phase portraits for the T38 resonant circuit at both $11\,\mathrm{kHz}$ and $12\,\mathrm{kHz}$. At all frequencies, the portraits begin at the origin and exhibit overshoot before ultimately settling into their respective steady-state periodic orbits. A comparison of the measured initial transient portion of the portraits are shown Fig. 12c for the M19 circuit and Fig. 14c for the T38 circuit. The simulated initial transients in Figs. 13c and 15c match the experimental results quite closely, although the simulated T38 circuit transient does not diverge quite as quickly as the measured case. The measured and simulated steady-state phase portraits are shown in Figs.12d and 13d for the M19 circuit and Figs. 14d and 15d for the T38 circuit.

The occurrence of the discontinuity can be understood by examining opposing positive and negative feedback effects in the resonant circuits. Start by considering the system at a very low frequency. An effective inductance can be calculated

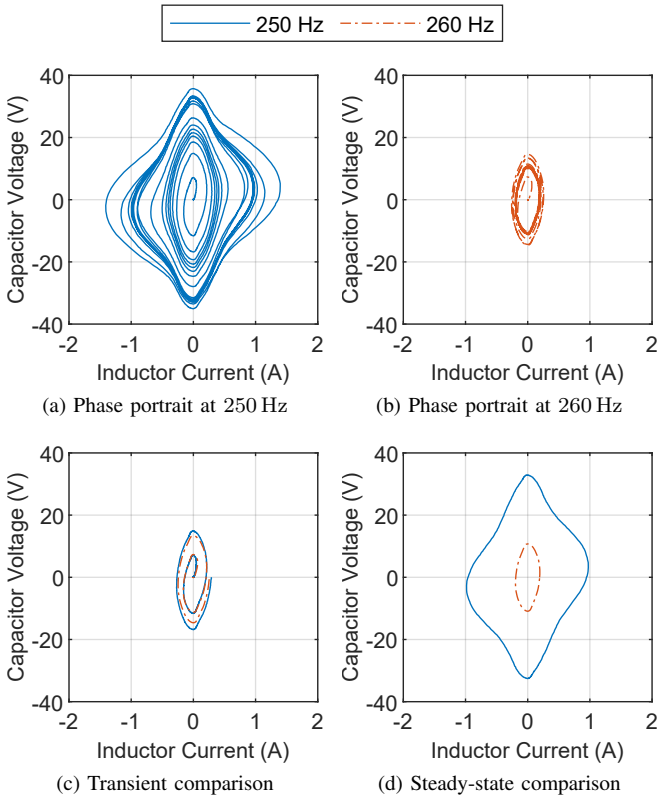

(a) Phase portrait at 250 Hz (b) Phase portrait at 260 Hz

(c) Transient comparison (d) Steady-state comparison

Fig. 12. Measured transient phase portraits for the M19 electrical steel resonant circuit at 250 Hz and 260 Hz for an input voltage of $5\,V_{RMS}$: (a) Full transient phase portrait at 250 Hz, (b) full transient phase portrait at 260 Hz, (c) comparison of the initial transients showing close of the initial trajectories over the first two cycles, and (d) comparison of steady-state behavior showing significantly different periodic orbits.

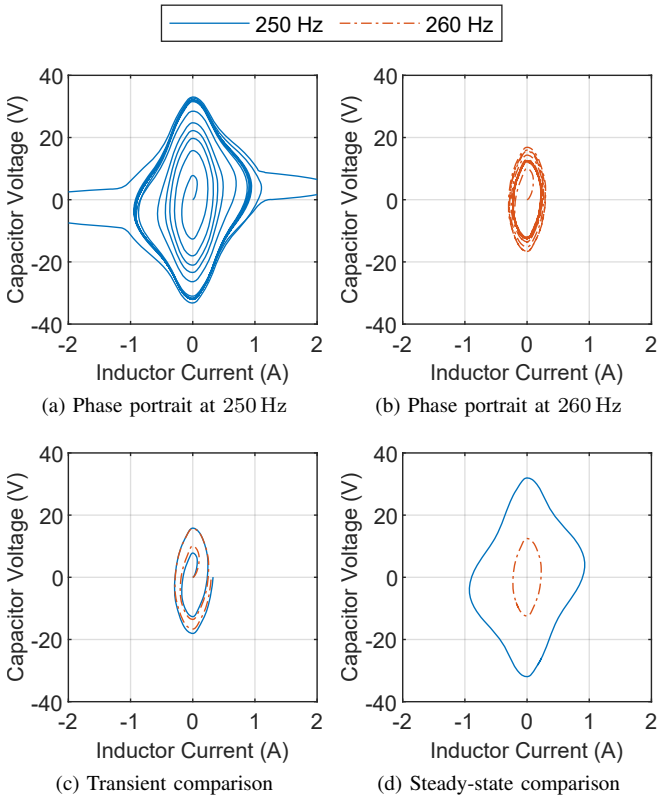

(a) Phase portrait at 250 Hz (b) Phase portrait at 260 Hz

(c) Transient comparison (d) Steady-state comparison

Fig. 13. Simulated transient phase portraits for the M19 electrical steel resonant circuit at 250 Hz and 260 Hz for an input voltage of $5\,V_{RMS}$: (a) Full transient phase portrait at 250 Hz, (b) full transient phase portrait at 260 Hz, (c) comparison of the initial transients showing close of the initial trajectories over the first two cycles, and (d) comparison of steady-state behavior showing significantly different periodic orbits.

around a nominal current trajectory and, along with the capacitor value, an apparent resonant frequency. Increasing the frequency slightly moves the system toward this apparent resonant peak. This will cause the inductor current to increase, pushing it closer to saturation, lowering the effective inductance, and further increasing the apparent resonant frequency.

As the frequency is varied this way, the system is, in a sense, chasing the resonant peak. However, inductor losses and therefore system damping also increase with frequency. Above the discontinuity frequency, the damping is large enough so that the system can no longer escape to the low inductance (high current) orbit, and the apparent resonant frequency exhibits a step decrease. This is evident from the phase portrait transient in Figs. 14c and 15c. At first, the 12 kHz spiral remains bounded by, but near, the 11 kHz spiral. After the initial transient, the 11 kHz portrait continues to increase its distance from the origin, whereas damping at 12 kHz prevents the system from increasing its amplitude any further. Thus, the portrait associated with the 12 kHz source frequency ultimately decays to a smaller amplitude orbit. A similar trend is observed when comparing the M19 transient behavior at 250 Hz and 260 Hz.

B. Bistable Operating Regimes

For a certain range of input voltages, the resonant circuits may operate at either a "low" or "high" amplitude orbit depending on the initial conditions that brought the system to the present state. One way of demonstrating this is to fix the operating frequency near the observed discontinuity in the nonlinear transfer functions and then vary the input voltage from a low value to a high value and back down again. This procedure was applied to both the M19 and T38 resonant circuits. The simulated and experimental results are given in Figs. 16a and 16b, respectively, showing the RMS inductor currents as a function of RMS input voltage amplitude and history.

The following mechanism can explain this behavior: As the voltage increases starting from a small value, more current is pushed through the inductor, lowering the inductance and increasing the apparent resonant frequency of the system. Eventually, positive feedback between the increasing inductor current and decreasing effective inductance causes a step change in the apparent resonant frequency from below the operating frequency to above it. The system transitions through a state of resonance, allowing a large current amplitude that locks the resonant frequency above the operating frequency.

After storing enough energy in the resonant tank, the system is able to maintain oscillations at a higher amplitude. As the input voltage decreases, the inductor current decreases and the apparent resonant frequency moves toward the operating frequency. The decrease in circuit impedance tends to offset the decrease in voltage so that the decrease in inductor current

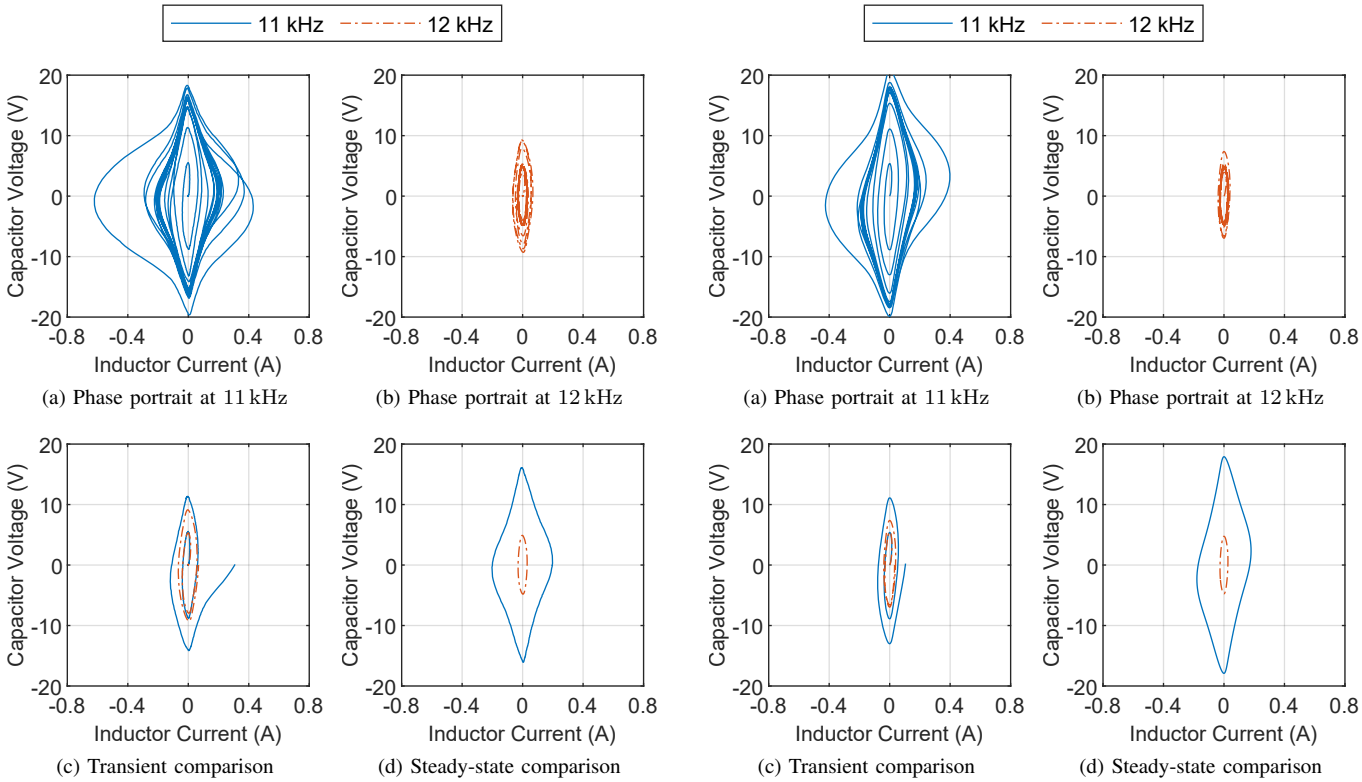

(a) Phase portrait at 11 kHz (b) Phase portrait at 12 kHz

(c) Transient comparison (d) Steady-state comparison

Fig. 14. Comparison of measured transient phase portraits for the T38 ferrite core resonant circuit at 11 kHz and 12 kHz for an input voltage of $3\,V_{RMS}$: (a) Full transient phase portrait at 11 kHz, (b) full transient phase portrait at 12 kHz, (c) comparison of the initial transients over the first two cycles demonstrating initial divergence of trajectories, and (d) comparison of steady-state behavior showing two different periodic orbits.

(a) Phase portrait at 11 kHz (b) Phase portrait at 12 kHz

(c) Transient comparison (d) Steady-state comparison

Fig. 15. Comparison of simulated transient phase portraits for the T38 ferrite core resonant circuit at 11 kHz and 12 kHz for an input voltage of $3\,V_{RMS}$: (a) Full transient phase portrait at 11 kHz, (b) full transient phase portrait at 12 kHz, (c) comparison of the initial transients over the first two cycles demonstrating initial divergence of trajectories, and (d) comparison of steady-state behavior showing two different periodic orbits.

is sublinear. Eventually, the apparent resonant frequency decreases below the operating frequency, the circuit impedance begins to increase, and the inductor current begins decreasing superlinearly. At some point, positive feedback between the falling inductor current and rising apparent inductance causes a step change to occur in the apparent resonant frequency of the system. This causes a step change in the circuit impedance, and the system falls to a lower amplitude oscillation.

The simulation models predict the existence of bistable operating regimes for both circuits. Qualitatively, the amplitude of the oscillations as represented by the RMS inductor current are captured quite accurately. The absolute location of the discontinuities with respect to applied voltage are less accurate, but still within the range of 10 %–20 %. The jump locations are likely very sensitive to modeling errors in the inductor cores at very high flux density levels. This type of error will greatly impact the initial transient behavior.

VII. Modeling Errors and Future Work

There are several known sources of error in the core models, particularly for the T38 core, which may explain some of the discrepancies between the simulations and experiments. First, the T38 core is much smaller and has fewer number of turns than the M19 core, which naturally introduces more uncertainty into the magnetic characterization process, especially at low field levels. This could be alleviated by using a larger toroid to gather material property data for simulating smaller cores. This introduces the question of material property variability, which must be examined nonetheless if the technique described here is to be used as a prognostic tool.

Second, the standard ferrite core dimensions described by the International Magnetics Association's IMA-STD-140 are not compatible with the dimensions required by the ASTM A773/A773M-01 ring core standard [22]. The ASTM requires, approximately, a ratio of mean core diameter to core thickness of greater than 10 to 1. Presumably, this is to limit the radial variation of the magnetic field intensity in the core to a small enough range so that any error can be effectively averaged out. Standard ferrite toroid cores have a ratio closer to 4 to 1, making them more susceptible to this systematic error. Additionally, ferrite toroids have chamfered corners that influence the field distribution and losses. These effects primarily impact the identification of the "knee" regions of the B-H curves, where the linear regime transitions to the saturated regime.

One possible solution is to the material identification issue would be to fabricate an ASTM standard–conforming ferrite toroids. The simulation challenge associated with nonuniform core cross sections can be resolved by generalizing the finite-element portion of the technique to allow geometrically mapped elements to handle more general core cross sections [20]. Another interesting proposal is to use the technique in this paper to iteratively solve the inverse

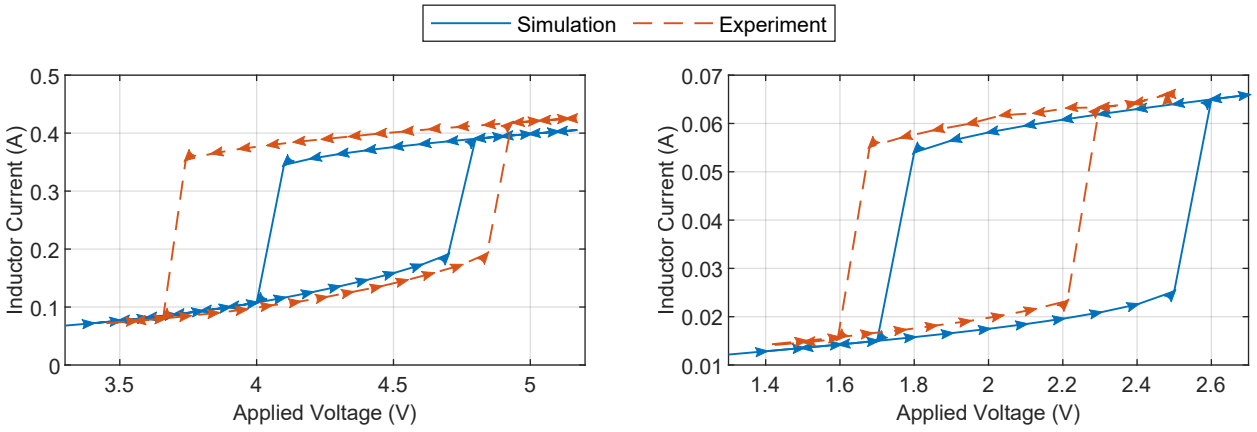

(a) M19 electrical steel resonant circuit at 250 Hz

(b) T38 ferrite resonant circuit operating at 10.7 kHz

Fig. 16. Simulated and measured bistability characteristics of two resonant circuits: The voltages are started at a low level and increased until a sharp jump in the RMS inductor current is observed. Then, the voltage is decreased until a sharp drop in the inductor is observed. Both circuits have regions where one of two steady-state conditions will be favored depending on the initial condition of the system.

problem of identifying the actual magnetic characteristics from the experimentally measured average magnetic characteristics.

The experimental validation in this paper has been performed in a way to eliminate, as much as possible, unmodeled high frequency effects in the experimental systems. The two main effects are AC winding losses and winding/core capacitance. AC winding losses will impact the quality factor of the resonant circuit when the conductor diameter is similar to the skin depth of copper at the operating frequency. Winding and core capacitances can modify the resonant frequency of the circuit and introduce additional resonant modes. In systems driven by square waves at higher frequencies (e.g. 100 kHz), parasitic capacitances can interact with harmonics generated by the source. Future work will focus on modeling AC winding losses and winding/core capacitances within the inductor finite-element simulation to capture these high-frequency effects.

VIII. Conclusion

This paper has presented a technique for high-fidelity modeling of toroid inductor magnetic and core loss properties along with experimental results validating the method. Two different cores were examined in the context of series RLC resonant circuits: one made from electrical steel laminations and one made from ferrite. Good agreement between simulation and experimental results was observed. The models demonstrated an ability to predict changes in the location of the circuit's resonant peak and associated quality factor, indicating an accurate representation of nonlinear inductance and losses over a wide range of input voltages and frequencies. The models also predicted discontinuities in the frequency response of the resonant circuits and bistable operating regimes resulting from opposing positive and negative feedback interactions caused by magnetic saturation and core losses.

Acknowledgments

The authors would like to thank the following people from Oak Ridge National Laboratory for their contributions to this work: Sheng Zheng and Zhiqiang (Jack) Wang for their assistance with the experimental setups and Burak Ozpineci for his managerial support. Additionally, the authors would like to thank Susan Rodgers for funding this work through the Department of Energy Vehicle Technology Office.

References

[1] A. Hubert and R. Schfer, *Magnetic Domains*. Springer, November 2008.
[2] G. Bertotti, *Hysteresis in Magnetism*. Academic Press, May 1998.
[3] D. Jiles, *Introduction to Magnetism and Magnetic Materials*, 3rd ed. CRC Press, September 2015.
[4] J. B. Goodenough, "Summary of losses in magnetic materials," *IEEE Transactions on Magnetics*, vol. 38, no. 5, pp. 3398–3408, Sep. 2002.
[5] I. Mayergoz, *Mathematical Models of Hysteresis and Their Applications*. Academic Press, August 2003.
[6] D. C. Jiles, "Modelling the effects of eddy current losses on frequency dependent hysteresis in electrically conducting media," *IEEE Transactions on Magnetics*, vol. 30, no. 6, pp. 4326–4328, Nov 1994.
[7] J. Lu, S. Yamada, and K. Bessho, "Time-periodic magnetic field analysis with saturation and hysteresis characteristics by harmonic balance finite element method," *IEEE Transactions on Magnetics*, vol. 26, no. 2, pp. 995–998, March 1990.
[8] J. W. Lu, S. Yamada, and H. B. Harrison, "Application of harmonic balance-finite element method (hbfem) in the design of switching power supplies," *IEEE Transactions on Power Electronics*, vol. 11, no. 2, pp. 347–355, March 1996.
[9] F. Cortial, F. Ossart, J. B. Albertini, and M. Aid, "An improved analytical hysteresis model and its implementation in magnetic recording modeling by the finite element method," *IEEE Transactions on Magnetics*, vol. 33, no. 2, pp. 1592–1595, March 1997.
[10] P. Rasilo, E. Dlala, K. Fonteyn, J. Pippuri, A. Belahcen, and A. Arkkio, "Model of laminated ferromagnetic cores for loss prediction in electrical machines," *IET Electric Power Applications*, vol. 5, no. 7, pp. 580–588, August 2011.
[11] L. A. R. Tria, D. Zhang, and J. E. Fletcher, "Implementation of a nonlinear planar magnetics model," *IEEE Transactions on Power Electronics*, vol. 31, no. 9, pp. 6534–6542, Sep. 2016.
[12] L. A. Righi, N. Sadowski, R. Carlson, J. P. A. Bastos, and N. J. Batislsla, "A new approach for iron losses calculation in voltage fed time stepping finite elements," *IEEE Transactions on Magnetics*, vol. 37, no. 5, pp. 3353–3356, Sep. 2001.
[13] K. Geldhof, P. Sergeant, A. V. den Bossche, and J. Melkebeek, "Analysis of hysteresis in resonance-based position estimation of switched reluctance drives," *IEEE Transactions on Magnetics*, vol. 47, no. 5, pp. 1022–1025, May 2011.
[14] A. Bermdez, L. Dupr, D. Gmez, and P. Venegas, "Electromagnetic computations with preisach hysteresis model," *Finite Elements in Analysis and Design*, vol. 126, pp. 65 – 74, 2017. [Online]. Available: http://www.sciencedirect.com/science/article/pii/S0168874X16302256

[15] P. Rasilo, W. Martinez, K. Fujisaki, J. Kyyr, and A. Ruderman, "Simulink model for pwm-supplied laminated magnetic cores including hysteresis, eddy-current, and excess losses," *IEEE Transactions on Power Electronics*, vol. 34, no. 2, pp. 1683–1695, Feb 2019.
[16] H. Lamba, M. Grinfeld, S. McKee, and R. Simpson, "Subharmonic ferroresonance in an lcr circuit with hysteresis," *IEEE Transactions on Magnetics*, vol. 33, no. 4, pp. 2495–2500, July 1997.
[17] E. Barbisio, O. Bottauscio, M. Chiampi, G. Crotti, and D. Giordano, "Parameters affecting ferroresonance in lcr electric circuits," *IEEE Transactions on Magnetics*, vol. 44, no. 6, pp. 870–873, June 2008.
[18] M. Dimian, P. Andrei, O. Manu, and V. Popa, "Comparison of noise-induced resonance characteristics for different models of hysteresis," *IEEE Transactions on Magnetics*, vol. 47, no. 10, pp. 3825–3828, Oct 2011.
[19] J. Pries, L. Tang, and T. Burress, "Continuum modeling of inductor hysteresis and eddy current loss effects in resonant circuits," in *2017 IEEE Energy Conversion Congress and Exposition (ECCE)*, Oct 2017, pp. 425–432.
[20] J. N. Reddy, *An Introduction ot the Finite Element Method*, 3rd ed. Mcgraw-Hill, 2006.
[21] ASTM International, "Standard test method for dc magnetic properties of materials using ring and permeameter procedures with dc electronic hysteresigraphs," West Conshohocken, PA, 2001, ASTM A773 / A77SM-01.
[22] The International Magnetics Association, "Standard specifications for ferrite toroid cores," Clevland, OH, 2011, IMA-STD-140.

Jason Pries (M'10) received the B.S. degree in electrical engineering from the Milwaukee School of Engineering, Milwaukee, WI, in 2009, and the M.S. and Ph.D. degrees in Electrical Engineering-Systems from the University of Michigan, Ann Arbor, MI, in 2012 and 2015, respectively.

He joined the Power Electronics and Electric Machinery Group at Oak Ridge National Laboratory, Oak Ridge, TN, as a Research and Development Associate Staff Member in 2015. His research interests revolve around magnetics, including the design and optimization of electric machines and wireless charging pads, high-fidelity modeling of magnetic materials and systems, and high-performance computing for electromagnetic eddy current problems.

Dr. Pries is the recipient of a Department of Energy Vehicle Technology Office Distinguished Achievement Award and UT-Battelle Research Accomplishment for his work on a non-rare earth electric motor. He is currently a Science Policy Fellow with the Society for Industrial and Applied Mathematics.

Emre Gurpinar (S'11–M'17) received the B.Sc. degree in electrical engineering from Istanbul Technical University, Istanbul, Turkey, in 2009, the M.Sc. degree in power electronics, machines, and drives from the University of Manchester, Manchester, U.K., in 2010, and the Ph.D. degree in electrical and electronics engineering from the University of Nottingham, Nottingham, U.K., in 2017.

From October 2011 to July 2013, he was a Research and Development Power Electronics Engineer with General Electric, Rugby, U.K. From August 2015 to October 2015, he was a Visiting Ph.D. Student in the Department of Energy Technology, Aalborg University, Aalborg, Denmark. In May 2017, he joined the Power Electronics and Electric Machinery Research Group at Oak Ridge National Laboratory, Knoxville, TN, USA, where he is working as R&D Staff. His current research focuses on power electronic systems, with special focus on wide-bandgap-based power semiconductor devices.

Lixin Tang (S'00–M'05–SM'08) was born in Yanzhou, Shandong province of China. He received the B.Eng. and M.Eng. degrees in electrical engineering from Nanjing University of Aeronautics and Astronautics, Nanjing, China, in 1991 and 1994, respectively, and the Ph.D. degree from the University of New South Wales (UNSW), Sydney, Australia in 2004.

From April 1994 to August 1998, he was with the Beijing Institute of Mechanical Equipment, working on static frequency converter project. In August 1998, he joined GE Hangwei Medical Systems Co. Ltd., Beijing, China as an electrical engineer where he worked on the x-ray generator (XG) subsystem of several CT scanners. He worked for Central Queensland University (CQU) as a post-doctoral research officer in Rockhampton, Australia from April 2004 to March 2005 after he finished his Ph.D. In April 2005, he joined Oak Ridge Associated Universities as a post-doctoral research associate and subsequently joined Oak Ridge National Laboratory as a power electronics engineer until 2017. He worked for Dynsity Technology Inc. as a senior motor control engineer from November 2017 to August 2017. He then joined Karma Automotive as a technical specialist on power electronics. His current research interests are xEV power electronics inverters, dc/dc converters, on-board chargers, and motor controls.

Dr. Tang has been senior member of IEEE since 2008. He received the First Prize Paper Award from the IEEE Industry Application Society (IAS) Industrial Power Converters Committee (IPCC) in 2008 and two Best Paper Awards at the 2009 and 2011 Vehicle Power and Propulsion Conference (VPPC'09, VPPC'11).

Timothy A. Burress (M'05–SM'18) received the B.S. and M.S. degrees in electrical engineering from the University of Tennessee, Knoxville, TN, USA, in 2004 and 2006, respectively.

From 2004 to 2006, he was Research Assistant at Oak Ridge National Laboratory. Since 2006, he has been a Research and Development Staff member leading and supporting electric machine design, fabrication, and comprehensive testing of motors for transportation, defense, and other applications. He also specializes in the development and implementation of hardware and software for robust motor feedback control systems.

Mr. Burress currently serves as Working Group Chair of the IEEE Industry Applications Society (IAS) and Power Electronics Society (PES) Working Group for the development of Standard 11, the IEEE Standard for Rotating Electric Machinery for Rail and Road Vehicles.